Wavelet-Compressed Representation of Landscapes for Hydrologic and Geomorphologic Applications

Chandana Gangodagamage, *Member, IEEE*, Efi Foufoula-Georgiou, Steven P. Brumby, Rick Chartrand, *Senior Member, IEEE*, Alexander Koltunov, Desheng Liu, Michael Cai, and Susan L. Ustin, *Senior Member, IEEE*

***Abstract*—The availability of high-resolution digital elevation data (submeter resolution) from LiDAR has increased dramatically over the past few years. As a result, the efficient storage and transmission of those large data sets and their use for geomorphic feature extraction and hydrologic/environmental modeling are becoming a scientific challenge. This letter explores the use of multiresolution wavelet analysis for compression of LiDAR digital elevation data sets. The compression takes advantage of the fact that, in most landscapes, neighboring pixels are correlated and thus contain some redundant information. The space–frequency localization of the wavelet filters allows one to preserve detailed high-resolution features where needed while representing the rest of the landscape at lower resolution. We explore a lossy compression methodology based on biorthogonal wavelets and demonstrate that, by keeping only approximately 10% of the original information (data compression ratio ∼94%), the reconstructed landscapes retain most of the information of relevance to geomorphologic applications, such as the ability to accurately extract channel networks for environmental flux routing, as well as to identify geomorphic process transition from the curvature–slope and slope–distance relationships.**

***Index Terms*—Biorthogonal modulation, biorthogonal wavelets, channel networks, data compression, Digital Elevation models (DEMs), high spatial resolution data, hydrology, image resolution, LiDAR, lossy compression, wavelets, wavelet transforms.**

I. Introduction

DATA compression [1] is extensively used in many applications where efficient storage and transmission of large data sets is needed and forms an area of active research in image processing and computer sciences. A compression algorithm is always accompanied by a decompression algorithm, which reconstructs the signal from its compressed form [2]. The decompression algorithm can be lossless (it reproduces the original signal exactly) or lossy (it reproduces the original signal to some approximation). How much information that can be affordably lost in the reconstructed signal depends on the application [2].

The most popular methodologies for data compression are based on wavelets [3]. Wavelets are a family of functions of compact support, all constructed from a mother wavelet by stretching or compressing it to change the size of the support window (scale). A wavelet transform projects the signal into the basis of the family of wavelet functions and computes the wavelet coefficients; multiplying those wavelet functions by the corresponding coefficients and summing them up reproduces the original signal [4]. We will take advantage of signal compression, where relatively smooth parts of an image (correlated neighboring pixels that contain redundant information) [5] result in small wavelet coefficients over a range of scales; setting these coefficients to zero reduces the information that must be carried in the signal without much loss of information in reproducing it.

Recently, a variety of powerful and sophisticated wavelet-based schemes for image compression have been developed and implemented. Because of the many advantages, the top competitors in the JPEG-2000 standard [6] are all wavelet-based compression algorithms. For example, the EZW algorithm is also a wavelet-based image compression algorithm [3] that can provide coarse signal approximations for fast data retrievals and rapid transmissions while progressively enhancing the quality of the image as more bits are transmitted or available. The EZW embedded coding approach offers this flexibility by grouping the bits in order of significance of the wavelet coefficients [3].

In image processing, compression is judged on the basis of the subjective and objective qualities of the reconstructed image. Objective criteria include signal-to-noise ratio, computational time needed for compression and decompression, and compression ratio. Subjective criteria include visual comparison of images. For hydrologic and geomorphologic applications, the aforementioned objective criteria might not be the most appropriate ones. Very high resolution digital topography (compared with the low-resolution DEMs at 30 m) offers opportunities for extracting more accurately and objectively channel heads and channel network organization [7]–[9], as well as identifying more objectively, and without the need

Manuscript received August 16, 2014; revised January 2, 2015; accepted January 26, 2015. Date of publication February 11, 2016; date of current version March 23, 2016.

C. Gangodagamage was with the Department of Land, Air and Water Resources, University of California, Davis, Davis, CA 95616 USA, with the Earth and Environmental Sciences and Space Science and Remote Sensing, Los Alamos National Laboratory, Los Alamos, NM 87544 USA. He is now with NOAA National Water Center, Tuscaloosa, AL 35406 USA (e-mail: chhandana@gmail.com).

E. Foufoula-Georgiou is with the Department of Civil Engineering, St. Anthony Falls Laboratory, and the National Center for Earth-surface Dynamics, University of Minnesota, Minneapolis, MN 55414 USA.

S. P. Brumby and R. Chartrand were with the Los Alamos National Laboratory, Los Alamos, NM 87545 USA. They are now with Descartes Labs, Los Alamos, NM 87544 USA.

A. Koltunov and S. L. Ustin are with the Department of Land, Air and Water Resources, University of California, Davis, Davis, CA 95616 USA.

D. Liu is with the Department of Geography, The Ohio State University, Columbus, OH 43210 USA.

M. Cai is with the Space Data Systems, Los Alamos National Laboratory, Los Alamos, NM 87545 USA.

Color versions of one or more of the figures in this paper are available online at http://ieeexplore.ieee.org.

Digital Object Identifier 10.1109/LGRS.2015.2513011

for field surveys, transitional regimes such as hillslope to valley to channel transition [10]–[13], high-center and low-center ice-wedge polygon formations in the arctic tundra landscape [14], [15], and landslide mantled landscapes [16]. In this letter, therefore, we evaluate the reconstructed landscapes on the basis of how well they reproduce relevant hydrological and geomorphological features.

This letter is structured as follows. In Section II, we present the theory behind the compression methodology we have used. In Section III, we apply the methodology to a real 2 km × 2 km landscape within a steep terrain of the South Fork Eel River basin, California. We present a comparison of the original and reconstructed landscapes in terms of the following: 1) ability to extract accurately the channel network and 2) reproduction of the slope–downstream distance relationship and the curvature–slope relationship. Finally, we discuss further extensions of the methodology that can be geared toward more specialized requirements of landscape reproduction.

II. Biorthogonal Wavelets

The wavelet transform of a function $f(x)$ is an integral transform with a family of functions called wavelets, i.e.,

$$Wf(a,b) = \int_{-\infty}^{\infty} f(x)\psi_{a,b}(x)dx = \langle f, \psi_{a,b}\rangle \tag{1}$$

where the wavelets $\psi_{a,b}$ are generated from a single function ψ, which is called the mother wavelet, by dilation and translation, i.e.,

$$\psi_{a,b}(x) = \frac{1}{\sqrt{a}}\psi\left(\frac{x-b}{a}\right). \tag{2}$$

The mother wavelet ψ satisfies the condition $\int \psi(x)dx = 0$, which implies that $\hat{\psi}(0) = 0$, making the wavelets a bandpass filter (e.g., [17]). Here, we use an orthonormal discrete wavelet transform, where the scale parameter a and the location parameter b are discretized on a dyadic scale, i.e., $a = a_0^m$ and $b = nb_0a_0^m$, where $a_0 = 2$, and $b_0 = 1$. Then, the function $f(x)$ can be reconstructed as

$$f(x) = \sum_m \sum_n C_{m,n}(f)\psi_{m,n}(x) \tag{3}$$

where

$$C_{m,n}(f) = \langle f, \psi_{m,n}\rangle \tag{4}$$

are the so-called wavelet coefficients.

Frequently, the decomposition and reconstruction of a function is done using the same orthonormal wavelet basis. This, however, limits the choice of wavelets. For example, if one wants a smooth wavelet (not the Haar wavelet, which is discontinuous and, as a result, has poor frequency localization) and a symmetric wavelet (to avoid boundary artifacts when using mirror boundary conditions), the choice is limited. However, if we relax the orthonormality condition, other choices of wavelets become possible, as, for example, using the so-called biorthogonal wavelets. In this case, the decomposition

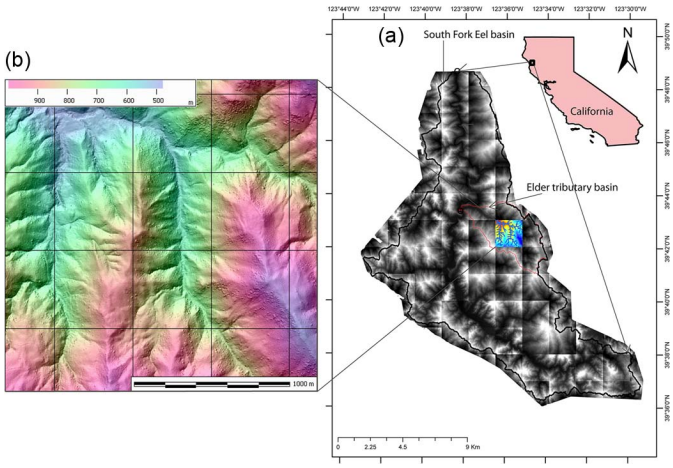

Fig. 1. (a) (top panel right) South Fork Eel River basin, California. (b) Analyzed 2 km × 2 km piece of the landscape (at 1-m resolution) within the (top panel left) Elder Creek subbasin.

is performed using the wavelets $\psi_{m,n}$, but the reconstruction is performed using the wavelets $\tilde{\psi}_{m,n}$, such that

$$\begin{aligned} f(x) &= \sum_m \sum_n < f,\ \psi_{m,n} > \tilde{\psi}_{m,n}(x) \\ &= \sum_m \sum_n < f,\ \tilde{\psi}_{m,n} > \psi_{m,n}(x). \end{aligned} \tag{5}$$

The wavelets $\psi_{m,n}$ and $\tilde{\psi}_{m,n}$ need to satisfy certain conditions (see, for example, [17] and [18]). A major advantage of biorthogonal wavelets is that one can have $\psi(t)$ and $\tilde{\psi}(t)$ with different vanishing moments. For example, if $\psi(t)$ has more vanishing moments than $\tilde{\psi}(t)$, one can obtain higher data compression rates while still achieving a very good reconstruction. Here, we use the Deslauriers and Dubuc biorthogonal wavelet [19] (for more details of the decomposition and reconstruction algorithm, the reader is referred to [17]).

III. Comparison of the Original and Reconstructed Landscapes

We analyzed a 2 km × 2 km piece within the Elder Creek subbasin of the South Fork Eel River basin [see Fig. 1(a) and (b)], for which LiDAR data at a resolution of 1 m × 1 m were available. Details about study sites location can be found in [12] and [20]. Fig. 2(a) shows a frequency histogram of the wavelet coefficients in the decomposition step. As shown in the figure, most of the wavelet coefficients are very small; 10^6 pixels have wavelet coefficients close to zero (a value of 1000 has been added to those coefficients for easier display), whereas only a very small number (on the order of 10) have higher values, which capture most of the information. Fig. 2(b) shows a zoom-in view to the zero-wavelet coefficients and shows that the values between -0.1 and 0.1 were set equal to zero in the reconstruction step (that value was chosen as the threshold on the wavelet coefficients to achieve an 88.6% compression ratio while still reproducing the major features of the analyzed landscape). Using biorthogonal Deslauriers–Dubuc wavelets [19] and the wavelet coefficient threshold, we reconstructed the landscape. The original and reconstructed landscapes are shown in

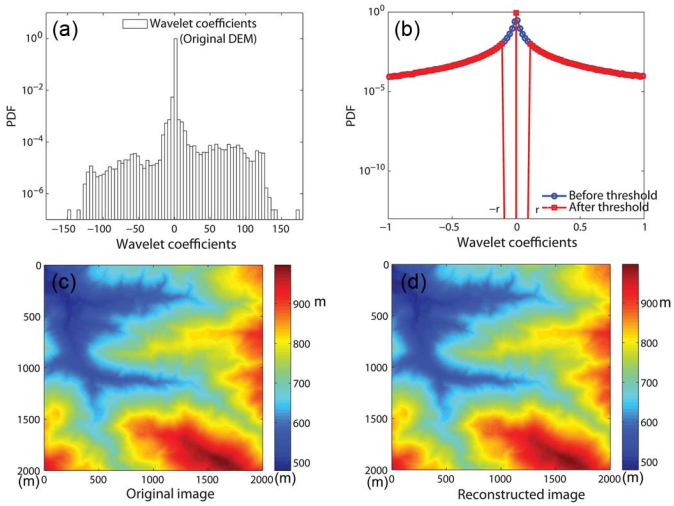

Fig. 2. (a) Probability density function of wavelet coefficients of the original landscape; notice that the vertical axis is in log scale and that most of the wavelet coefficients are close to zero with only a small percentage having large values. (b) Zoom-in view of the wavelet coefficients close to zero; the marked area shows the wavelet coefficients of magnitudes between -r and r ($\sim -0.1 - 0.1$), which were set to zero during the reconstruction. (c) Elevation map of the original 1-m resolution landscape. (d) Reconstructed landscape using wavelet compression using the threshold shown in (b).

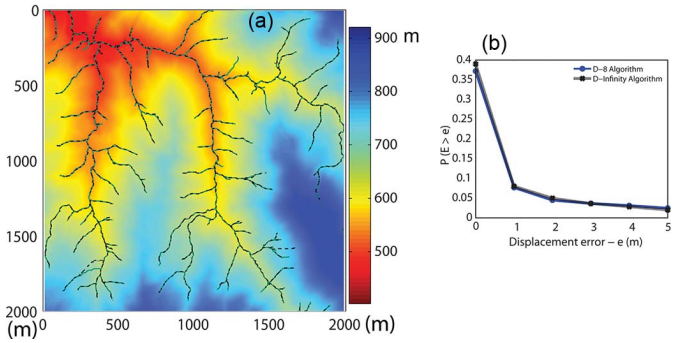

Fig. 3. (a) Superposition of the river network extracted from the (light green thick line) original LiDAR data and the (black dashed line) one extracted from the reconstructed topography. On average, the channel initiation points derived using the area threshold method ($A_{tr} = 1000\ m^2$) were located further away from the hillslopes in the reconstructed DEM compared with the original DEM. This suggests that in the hillslopes and valleys are where the reconstruction has mostly altered the convergence of flow paths and thus the computed contributing area. (b) Exceedence probability of the horizontal displacement error between the river network extracted from the original and reconstructed topographies as shown in (a).

Fig. 2(c) and (d), respectively. One can hardly detect any visible difference between the two landscapes, although the compression ratio of approximately 87% means that only 13% of the wavelet coefficients were kept in the reconstruction.

Fig. 3(a) shows the extracted channel network using the original and reconstructed landscapes. Channels were initiated using a simple threshold area criterion, in this case, an area of 1000 m^2, and the D8 algorithm of steepest gradient was used to delineate the channels [21]. The two networks are very close to each other, with most of the differences appearing in the channel head initiation. The D-infinity flow resolving algorithm was also used to delineate the river network for the same areas [22]. As will be shown later, it is exactly in the nonconvergent and slightly convergent areas (hillslopes to hollows) where most of the wavelet coefficients were set to zero during the

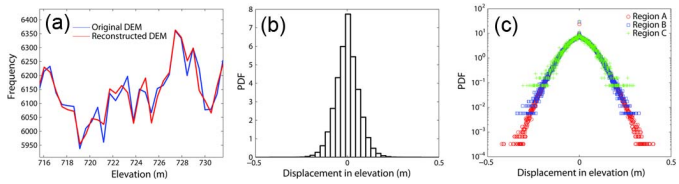

Fig. 4. (a) Elevation difference in reconstructed and original DEMs is shown as number of times that each elevation value between 716 and 735 m is occurring spatially in the 2 km × 2 km DEM. (b) Probability distribution of the elevation error is given. (c) Distribution of elevation displacement in regions A, B, and C, which are classified based on the topographic regimes defined in [8].

reconstruction and thus the locations where the reconstructed landscape differs most from the original landscape. Fig. 3(b) shows that 63% of the points of the two extracted networks coincide with each other, whereas 97.6% are within 5 m of horizontal displacement. A comparison between the D-8 and D-infinity algorithms for the channel network delineations in original and reconstructed landscapes is also given in Fig. 3(b). While 98.1% in channel points using D-infinity algorithm are within 5 m of horizontal distance, approximately 61% of points in the extracted networks coincide with each other.

Fig. 4(a) shows the elevation density function of the original and reconstructed landscapes; one can hardly see any differences in this plot. However, the probability density of the elevation differences between the original and reconstructed landscapes (here referred to as displacement elevations) is shown in Fig. 4(b). Most show zero difference (perfect reconstruction), whereas some elevations have errors on the order of $\pm$10–20 cm after the reconstruction. The mean vertical error associated with the reconstructed landscape is 6.7 cm, which is within the vertical error of the LiDAR data (i.e., $\sim$15 cm). The displacement errors in the reconstructed landscape associated with regions A, B, and C are shown in Fig. 4(c). The nonconvergent and slightly convergent landscapes (regions A and B) show the largest discrepancies in elevations compared with fluvial network (region C).

It is interesting to probe further and understand exactly where in the landscape most of the errors occurred during the reconstruction process. For this, we perform a detailed analysis of the curvatures, contributing areas, and local slopes for the analyzed part of the landscape. Fig. 5(a) shows the local slope versus directed distance from the divide [12]. From this plot, three distinct regions are identified: region A, which corresponds to divergent or planar flow paths, region B, which corresponds to convergent network hollows, and region C, which corresponds to the fluvial part of the river basin. As shown in Fig. 5(a), no major differences are detected in the gradients of the original and reconstructed landscapes. However, the computed curvatures differ much more, as shown in Fig. 5(b). Specifically, the curvatures of the reconstructed landscape are smaller than that of the original landscape, as expected, since setting 87% of the wavelets to zero resulted in "flatter" landscapes in terms of local curvature. The same effect is seen in the typical curvature–local slope plot in Fig. 5(c). Most of the spatially distributed differences are observed in regions A and B, which are the unchannelized parts of the basin. Fig. 5(d) shows the local slope versus contributing area for the original and reconstructed landscapes in which the reconstructed landscape shows relatively low flow accumulations in region B.

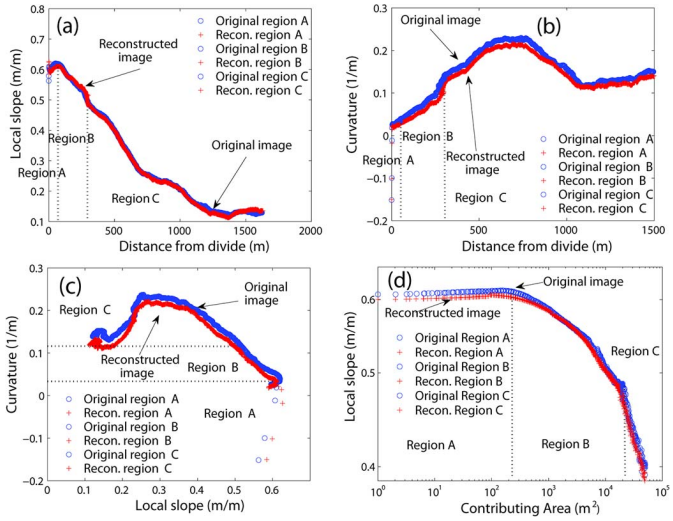

Fig. 5. (a) Slope as a function of distance measured from the ridge lines for the original (blue color, o) and reconstructed (red color, +) landscapes for regions A, B, and C, respectively. (b) Curvature as a function of distance measured from the ridge lines for the original and reconstructed landscapes for regions A, B, and C. (c) Slope–curvature plot parameterized by distance measured from ridge lines. (d) Slope as a function of contributing area for the original (blue color, o) and reconstructed (red color, +) landscapes for regions A, B, and C, respectively.

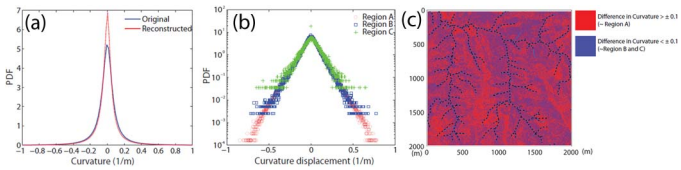

Fig. 6. (a) Probability distribution of the curvature of the original and reconstructed DEMs. (b) Curvature displacement in regions A, B, and C. (c) Spatial distribution of the curvature differences between the original and reconstructed DEMs. The red color shows the area where the difference in curvature is larger than the values of −0.1 and 0.1. The blue color corresponds to the areas where the magnitude of curvature differences is between 0.1 and −0.1. The red color area mainly represents region A, and the blue color area represents regions B and C.

It is instructive to analyze the statistical properties of the curvature, and this analysis is shown in Fig. 6(a) for the original and reconstructed landscapes overall, as well as regions A, B, and C in Fig. 6(b). As expected, the largest discrepancies in the computed curvatures are in the nonchannelized parts of the landscape (regions A and B), which is further shown in Fig. 6(c), which displays the exact locations where most of the curvature differences between the original and reconstructed landscapes are found.

Fig. 7(a) shows a plot of the contributed area as computed from the original and reconstructed landscapes. One can hardly see any difference between the two curves. However, zooming in to small contributing areas (in regions A and B), one can see that the reconstructed landscapes result in smaller computed contributed areas compared with those computed from the original landscapes [see Fig. 7(b)]. This is not surprising as it is in these regions that the curvature of the reconstructed landscapes was found smaller than those of the original landscapes, which affected the degree of convergence of flow paths most, due to compression and reconstruction. As expected, larger differences in contributing area were not observed [see Fig. 7(c)]. Choosing different wavelets or allowing for a smaller

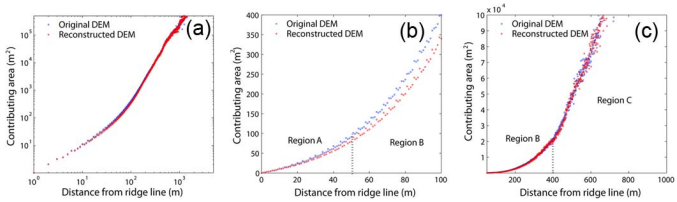

Fig. 7. (a) Contributing area is plotted against the distance measured from ridgelines for the original and reconstructed landscapes. (b) Zooming into the small contributing areas, one sees that there is a considerable difference in the contributing areas for the planar and slightly convergent parts of the landscape (regions A and B). (c) As one goes to larger areas, the flow paths extracted from the original and reconstructed landscapes coincide, resulting in minimal differences in the extracted values of contributing areas.

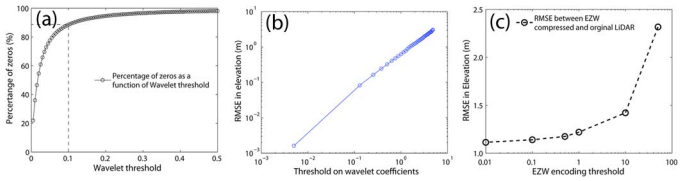

Fig. 8. (a) Percentage of wavelet coefficients was set to zero as a function of wavelet thresholds. (b) RMSE of the reconstructed DEM using BZW approach as a function of wavelet threshold. (c) Comparison of wavelet-based DEM compression using EZW algorithms is plotted, and the rmse is computed in the reconstructed DEM as a function of encoding threshold.

compression ratio could alleviate this problem, and this needs to be further investigated.

Finally, one specific parameter of interest is the compression ratio in terms of number of wavelet coefficients that set into zero and the resulting data compression that is associated with the encoding of zero runs in the final reconstructed landscape specifically for data storage and transmission purposes. Fig. 8(a) shows a plot of root-mean-square error (rmse) in elevation as a function of available wavelet coefficients for the reconstruction process. As more detailed bits are progressively available for the reconstruction process, rmse of the reconstruction landscape gradually showed a better agreement with the LiDAR elevations of the original landscape. When all the wavelet coefficients that are less than ± 0.1 (i.e., $-0.1 <$ wavelet coefficients < 0.1) are set to zero, our algorithm, which we called biorthogonal zero-run wavelet (BZW) compression algorithm, showed 6-cm vertical rmse [see Fig. 8(b)] in the reconstructed landscape.

Instead of coding the individual wavelet coefficient values, it is more efficient to code the runs of zeros and other nonzero values. In our coding, all pixels set to "zero" are further encoded using a run-length lossless compression (RLC) algorithm. Using run-length encoding, we stored the occurrences of zeros as a single value and count (i.e., "0" and number of occurrence of "0"), rather than just the original run; hence, the run length of zeros represented the number of consecutive zeros between other nonzero values and the count in each run. Therefore, it is advantageous to encode the runs of zeros using RLC, rather than using each zero-valued coefficient individually. We multiplied the wavelet coefficients from 10^4 and then converted all the wavelet coefficients to 32-bit-long integers and applied the RLC algorithm. The average run length for zeros is approximately 18, whereas the average run length for nonzeros is approximately 1. Nearly no compression of the nonzero wavelet coefficients has been observed. The BZW algorithm achieved

approximately 94% of data compression ratio for the LiDAR DEM compression.

A comparison of the BZW approach with other lossy compression approaches that are currently used in natural image and DEM compressions is shown in Fig. 8(c). For this purpose, we used an EZW algorithm [3]. The EZW algorithm is a progressive encoding algorithm, wherein which, when more bits are added to the stream, the accuracy of the reconstructed landscape is improved. We changed the encoding threshold from 0.01 to 50, and the computed rmses for the reconstructed LiDAR DEMs are shown in Fig. 8(c). The lowest rmse observed was 1.20 m. The computation cost for the lowest threshold was approximately 20 h for a 2048×2048 pixel floating-point DEM in Intel i7 central processing unit.

IV. Discussion

Many natural signals have shown concise representation when expressed in an appropriate basis. While nearly all the image pixels have nonzero values, the wavelet coefficients offer a concise summary in which most coefficients are small and relatively few large coefficients capture most of the information. This fact has been well established for natural images, but how such compressed forms of high-resolution DEMs influence the hydrologic and geomorphic properties of landscape such as elevation, slope, curvature, flow accumulation, and flow convergence has not been well studied. When a DEM has a sparse representation, one can discard the small coefficients without much noticeable perceptual loss. Data compression implemented here takes advantage of the fact that, in most landscapes, neighboring pixels are correlated and thus contain some redundant information that can be effectively compressed without affecting the hydrologic and geomorphic properties of the DEM data set. We did a detailed comparison of discrepancies that are associated with the reconstructed image based on the landscape regimes documented in Gangodagamage *et al.* [12]. The total displacement of river network (region C) that exceeds 5 m from the original DEM is less than 0.05. The reconstructed image showed largest curvature displacement in regions A and B, whereas only minor displacement was observed in region C. There are considerable differences in contributing area for planar (region A) and slightly convergent (region B) parts of the landscape, whereas for larger areas, the contributing areas extracted from the original and reconstructed landscapes coincide with each other. After encoding the elevation values using the BZW approach, we documented 94% compression ratio for the floating-point LiDAR with 6-cm rmse. We only compressed the wavelet coefficients that are set to zero, and no compression was observed in other nonzero floating-point wavelet coefficients.

V. Conclusion

We have explored the application of wavelet compression methodologies for reducing the storage and information in high-resolution floating-point digital elevation topography available from LiDAR (0.5- to 1-m resolution). It was shown that, by using biorthogonal wavelets, one can achieve a high compression ratio (on the order of 87%) while achieving a very faithful reconstruction of most of the geomorphic attributes of the original landscape. Further research should explore how these compressed landscapes can be used to advance landscape evolution modeling, i.e., how one could perform a topographic elevation update, not at every grid point, but only at a reduced percentage of the DEM points where most of the flux transport takes place. This would be a considerable advantage for scientific and engineering computations and simulations where landscapes of large spatial extent are evolved over long periods of time to assess how different climatic and human-imposed perturbations propagate through the system from smaller to larger scales and vice versa.

References

[1] N. F. Thornhill, M. A. A. S. Choudhury, and S. L. Shah, "The impact of compression on data-driven process analyses," *J. Process Control*, vol. 14, no. 4, pp. 389–398, Jun. 2004.

[2] D. Salomon, *Data Compression*. New York, NY, USA: Springer-Verlag, 2000, p. 879.

[3] J. M. Shapiro, "Embedded image coding using zerotrees of wavelet coefficients," *IEEE Trans. Signal Process.*, vol. 41, no. 12, pp. 3445–3462, Dec. 1993.

[4] I. Daubechies, *Ten Lectures on Wavelets*, vol. 357. Philadelphia, PA, USA: Soc. Ind. Appl. Math., 1992.

[5] C. Gangodagamage, C. X. Zhou, and H. S. Lin, "Autocorrelation—Spatial," in *Encyclopedia of GIS* S. Shekhar and H. Xiong, Eds. New York, NY, USA: Springer-Verlag, 2008, pp. 32–37.

[6] D. S. Taubman and M. W. Marcellin, *JPEG 2000 Image Compression Fundamentals, Standards and Practice*. Norwell, MA, USA: Kluwer, 2001.

[7] B. Lashermes, E. Foufoula-Georgiou, and W. Dietrich, "Channel network extraction from high resolution topography using wavelets," *Geophys. Res. Lett.*, vol. 34, Oct. 2007, Art. ID L23S04.

[8] P. Passalacqua, T. D. Trung, E. Foufoula-Georgiou, G. Sapiro, and W. E. Dietrich, "A geometric framework for channel network extraction from LiDAR: Nonlinear diffusion and geodesic paths," *J. Geophys. Res.*, vol. 115, Jan. 2010, Art. ID F01002.

[9] C. Gangodagamage, E. Foufoula-Georgiou, and P. Belmont, "River basin organization around the main stem: Scale invariance in tributary branching and the incremental area function," *J. Geophys. Res. Earth Surf.*, vol. 119, no. 10, pp. 2174–2193, Oct. 2014.

[10] P. Tarolli and G. D. Fontana, "Hillslope-to-valley transition morphology: New opportunities from high resolution DTMs," *Geomorphology*, vol. 113, no. 1/2, pp. 47–56, Dec. 2009.

[11] P. Tarolli, "High-resolution topography for understanding Earth surface processes: Opportunities and challenges," *Geomorphology*, vol. 216, pp. 295–312, Jul. 2014.

[12] C. Gangodagamage, P. Belmont, and E. Foufoula-Georgiou, "Revisiting scaling laws in river basins: New considerations across hillslope and fluvial regimes," *Water Resour. Res.*, vol. 47, Jul. 2011, Art. ID W07508.

[13] I. Rodriguez-Iturbe and A. Rinaldo, *Fractal River Networks: Chance and Self-Organization*. New York, NY, USA: Cambridge Univ. Press, Aug. 1997, p. 540.

[14] C. Gangodagamage *et al.*, "Extrapolating active layer thickness measurements across Arctic polygonal terrain using LiDAR and NDVI data sets," *Water Resour. Res.*, vol. 50, no. 8, pp. 6339–6357, Aug. 2014.

[15] S. S. Hubbard *et al.*, "Relating subsurface and land-surface variability in permafrost environments using surface geophysical and LiDAR datasets," *Hydrogeol. J.*, vol. 21, no. 1, pp. 149–169, Feb. 2013.

[16] C. Gangodagamage, E. Foufoula-Georgiou, P. Belmont, B. H. Mackey, and T. K. Fuller, "Statistical signature of deep-seated landslides," American Geophysical Union Fall Meeting, San Francisco, CA, USA, Dec. 2014.

[17] S. Mallat, *A Wavelet Tour of Signal Processing*. San Diego, CA, USA: Academic, 1998, p. 795.

[18] P. Kumar and E. Foufoula-Georgiou, *Wavelet Analysis in Geophysics: An Introduction Wavelets in Geophysics*. New York, NY, USA: Academic, Sep. 1994, p. 373.

[19] G. Deslauriers and S. Dubuc, "Symmetric iterative interpolation processes, constructive approximations," *Constructive Approx.*, vol. 5, no. 1, pp. 49–68, Dec. 1989.

[20] C. Gangodagamage, E. Barnes, and E. Foufoula-Georgiou, "Scaling in river corridor widths depicts organization in valley morphology," *Geomorphology*, vol. 91, pp. 198–215, Nov. 2007.

[21] J. O'Callaghan and D. Mark, "The extraction of channel networks from digital elevation data," *Comput. Vis. Graph. Image Process.*, vol. 28, pp. 328–344, Dec. 1984.

[22] D. G. Tarboton, "A new method for the determination of flow directions and upslope areas in grid digital elevation models," *Water Resour. Res.*, vol. 33, no. 2, pp. 309–319, Feb. 1997.